Quaternary Science Reviews 266 (2021) 107052

Contents lists available at ScienceDirect

Quaternary Science Reviews

journal homepage: www.elsevier.com/locate/quascirev

Stratigraphic evidence of two historical tsunamis on the semi-arid coast of north-central Chile

Jessica M. DePaolis [a, *], Tina Dura [a, b], Breanyn MacInnes [c], Lisa L. Ely [c], Marco Cisternas [d], Matías Carvajal [d], Hui Tang [e], Hermann M. Fritz [f], Cyntia Mizobe [d], Robert L. Wesson [g], Gino Figueroa [d], Nicole Brennan [h], Benjamin P. Horton [i, j], Jessica E. Pilarczyk [k], D. Reide Corbett [l], Benjamin C. Gill [a], Robert Weiss [a, b]

[a] Department of Geosciences, Virginia Polytechnic Institute and State University, Blacksburg, VA, USA
[b] Center for Coastal Studies, Virginia Polytechnic Institute and State University, Blacksburg, VA, USA
[c] Department of Geological Sciences, Central Washington University, Ellensburg, WA, USA
[d] Instituto de Geografía, Pontificia Universidad Católica de Valparaíso, Valparaíso, Chile
[e] German Research Centre of Geosciences, Potsdam, Germany
[f] School of Civil and Environmental Engineering, Georgia Institute of Technology, Atlanta, GA, USA
[g] Geologic Hazards Science Center, U.S. Geological Survey, Denver, CO, USA
[h] Department of Geosciences, University of Rhode Island, Kingston, RI, USA
[i] Asian School of the Environment, Nanyang Technological University, Singapore
[j] Earth Observatory of Singapore, Nanyang Technological University, Singapore
[k] Centre for Natural Hazards Research, Department of Earth Sciences, Simon Fraser University, Burnaby, BC, Canada
[l] Department of Coastal Studies, East Carolina University, Wanchese, NC, USA

ARTICLE INFO

Article history:
Received 31 March 2021
Received in revised form
15 June 2021
Accepted 20 June 2021
Available online xxx

Handling Editor: I Hendry

Keywords:
North-central Chile
Earthquakes
Paleotsunamis
Tsunami inundation
Coastal hazards

ABSTRACT

On September 16, 2015, a M_w 8.3 earthquake struck the north-central Chile coast, triggering a tsunami observed along 500 km of coastline, between Huasco (28.5°S) and San Antonio (33.5°S). This tsunami provided a unique opportunity to examine the nature of tsunami deposits in a semi-arid, siliciclastic environment where stratigraphic and sedimentological records of past tsunamis are difficult to distinguish. To improve our ability to identify such evidence, we targeted one of the few low-energy, organic-rich depositional environments in north-central Chile: Pachingo marsh in Tongoy Bay (30.3°S).

We found sedimentary evidence of the 2015 and one previous tsunami as tabular sand sheets. Both deposits are composed of poorly to moderately sorted, gray-brown, fine-to medium-grained sand and are distinct from underlying and overlying organic-rich silt. Both sand beds thin (from ~20 cm to <1 cm) and fine landward, and show normal grading. The older sand bed is thicker and extends over 125 m further inland than the 2015 tsunami deposit. To model the relative size of the tsunamis that deposited each sand bed, we employed tsunami flow inversion. Our results show that the older sand bed was produced by higher flow speeds and depths than those in 2015. Anthropogenic evidence along with ^{137}Cs and ^{210}Pb dating constrains the age of the older tsunami to the last ~110 years. We suggest that the older sand bed was deposited by the large tsunami in 1922 CE sourced to the north of our study site. This deposit represents the first geologic evidence of a pre-2015 tsunami along the semi-arid north-central Chile coast and highlights the current and continuing tsunami hazard in the region.

1. Introduction

The coast of north-central Chile (30–32°S) lies along a seismically active portion of the Chilean subduction zone that has produced multiple > M8 earthquakes over the last few centuries (Métois et al., 2013). The most recent megathrust earthquake in north-central Chile occurred on September 16, 2015 (M_w 8.3) and produced a destructive tsunami that affected ~500 km of coastline (Fig. 1). During the 2015 earthquake, tsunami heights (the elevation reached by tsunamis relative to the still sea level) reached ~2 m at

* Corresponding author.
E-mail address: jessicad@vt.edu (J.M. DePaolis).

https://doi.org/10.1016/j.quascirev.2021.107052

most tidal stations within the rupture area and exceeded 4 m at Coquimbo (30°S; Barnhart et al., 2016; Contreras-Lopez et al., 2016). Modeled vertical displacement of the coast along the rupture area was relatively low, with ~40 cm of subsidence between 30.5 and 31°S and ~10–15 cm of uplift to the north and south (Barnhart et al., 2016). Historical records document previous earthquakes with rupture extents similar to that of the 2015 in 1880 and 1943 CE; however written accounts from these two earthquakes report somewhat lower tsunami heights, most less than 4 m (Lomnitz, 1970). Prior to the 2015 tsunami, the highest tsunami documented in historical records in north-central Chile was produced by the 1922 earthquake that ruptured the megathrust fault segment to the north (between ~26 and 30°S). According to limited observations, maximum tsunami heights were ~5–~9 m along ~350 km of coastline from Chañaral (26.5°S) to Coquimbo (Fig. 1; Lomnitz, 1970; Carvajal et al., 2017a). Despite the historical records of earthquakes and tsunami impacts in north-central Chile, direct observations are sparse and focused in populated areas, leaving uncertainty about the spatial variability of past ruptures and the extent and size of their accompanying tsunamis (Fig. 1d).

Coastal geologic datasets of earthquakes and tsunamis on centennial and millennial timescales capture rare but catastrophic events and so improve our ability to assess subduction zone hazards (Cisternas et al., 2005; Nelson et al., 2020; Philibosian and Meltzner, 2020; Sawai, 2020). Coastal stratigraphic sequences in low-energy depositional environments can record sudden changes in relative sea level (RSL) during coseismic deformation of the coast, sometimes in combination with widespread sand beds deposited by tsunamis accompanying large subduction zone earthquakes (Atwater, 1987; Dura et al., 2016; Engel et al., 2020). Anomalous sand beds deposited by tsunamis can also be preserved onshore in the absence of evidence of vertical deformation of the coast, depending on the proximity of the earthquake source to the coastline and the coastal morphology and depositional environments of the region, for example (Cisternas et al., 2017; Dura et al., 2017; Kelsey et al., 2002; Satake and Atwater, 2007).

Such coastal studies have documented stratigraphic evidence of great subduction zone earthquakes within tidal marshes in southern (Cisternas et al., 2005, 2017; Garrett et al., 2015), south-central (Dura et al., 2017; Ely et al., 2014; Hong et al., 2017), and

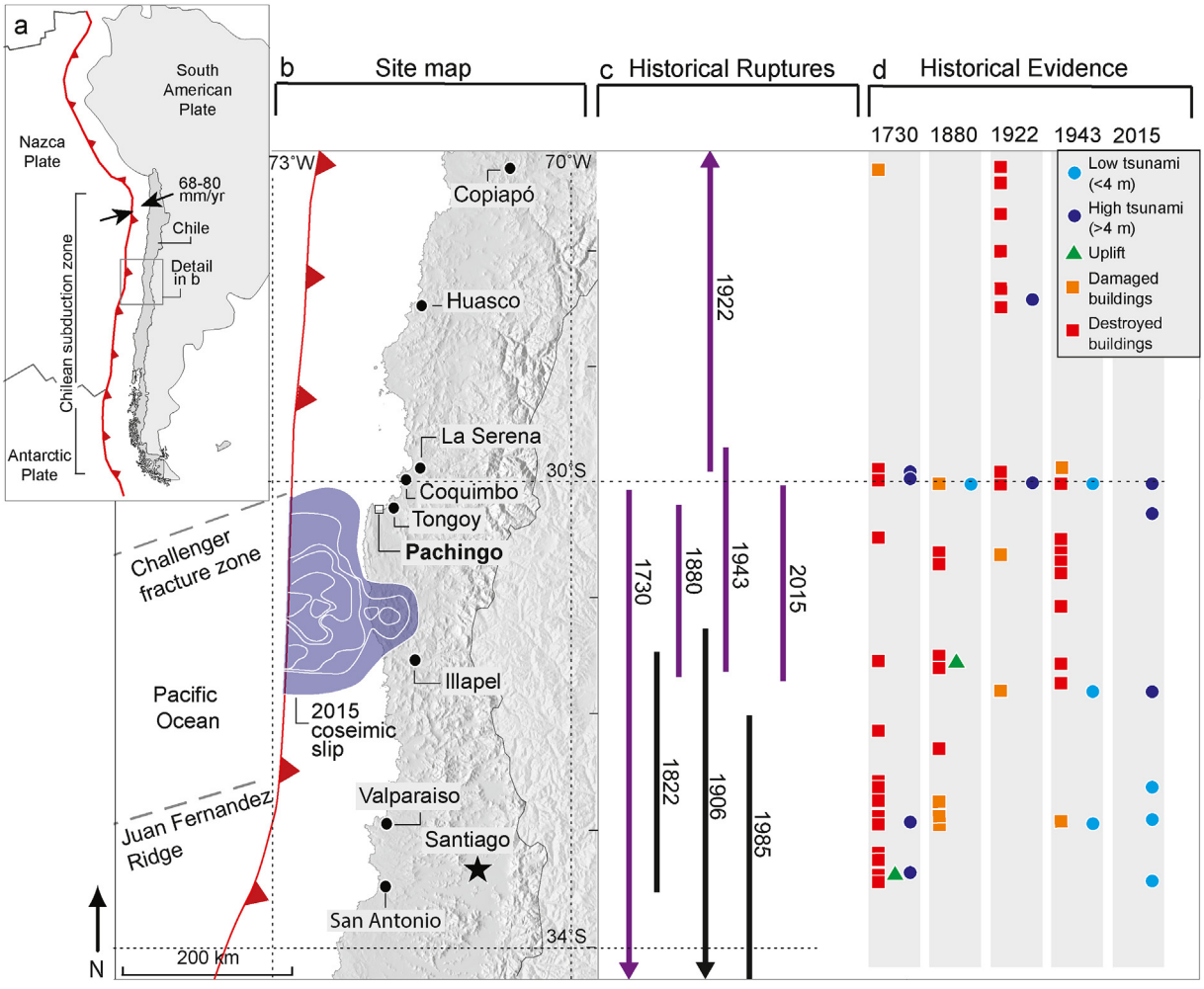

Fig. 1. Index maps, a) Plate-tectonic setting of Chile in western South America, b) Location of the study area in north-central Chile and main tectonic features. The highly coupled zone of the Chilean subduction zone is between 30°S and 32°S. The 2015 north-central Chile earthquake peak slip (with 1 m contours) is shown offshore in purple (Barnhart et al., 2016). c) Estimated rupture lengths of the largest historical earthquakes in central and north-central Chile since 1730 CE shown by solid purple (refer to years shown in d) and black lines - all lengths are inferred except for the 2015 event. Ruptures compiled from Lomnitz (1970), Comte et al. (1986), Beck et al. (1998), Melnick et al. (2009), Udias et al. (2012), Melnick et al. (2012), Barnhart et al. (2016), and Cisternas et al. (2017). d) Summary of historical and paleoseismic evidence for ruptures along the north-central portions of the subduction zone over the last ~300 years. Symbols represent historical accounts of damage, uplift, or tsunami height from each of the events. Building damage has not been compiled for the 2015 earthquake. Squares represent damaged (orange) and destroyed (red) buildings, triangle represents uplift, and circle represents lesser (light blue) and larger (dark blue) tsunami height measurements at different coastal locations. Historical records summarized by Lomnitz (1970), Cisternas et al. (2005, 2017), and Udias et al. (2012).

central (Dura et al., 2015; Nentwig et al., 2018) Chile enabling the development of earthquake histories over multiple earthquake cycles. However, in north-central Chile, the combination of a semi-arid, rocky coastline dominated by siliciclastic rather than organic-rich sediment, and net Holocene RSL emergence has resulted in few low-energy depositional environments in which to preserve stratigraphic evidence of coseismic deformation or tsunami inundation. Similar challenges in documenting stratigraphic evidence of tsunamis have been encountered on other semi-arid to hyper-arid coastlines (i.e., Northern Chile, Peru, Oman, etc.) (Donato et al., 2009; Spiske et al., 2013a,b; Soto et al., 2014; Dura et al., 2015; León et al., 2019). Despite these limitations, the recent 2015 tsunami provided an opportunity to investigate the geologic signature of tsunami inundation along the coastline of north-central Chile, and served as a guide for locating sites that may contain longer records of past tsunami inundation of this coast.

Here, we present the first compelling stratigraphic evidence of pre-2015 tsunami inundation along the coast of north-central Chile. In Pachingo marsh (30.3°S), we employ sedimentological, dating (^{137}Cs and ^{210}Pb), geochemical, and historical analyses, as well as tsunami flow inversion to compare the 2015 tsunami deposit to an older sand bed preserved at the site, and show that the older sand bed was likely deposited by a comparable or even higher tsunami than in 2015. Our discovery provides additional insight into the type of ruptures that create high tsunamis along the north-central Chile coast and demonstrates how careful site selection and a multidisciplinary (e.g., stratigraphic, historical, and modeling) approach may help improve earthquake and tsunami histories along similar arid subduction zone coastlines.

2. Subduction zone coastal setting

2.1. Earthquake history of north-central Chile

The Chilean subduction zone extends 3500 km along the western coast of Chile, marking the plate boundary between the subducting Nazca plate and the overriding South American plate (Fig. 1a). In north-central Chile, the Nazca plate subducts obliquely (10-20°-angle from trench-normal convergence) at a rate of 68–80 mm/yr (Métois et al., 2013; Pardo et al., 2002). Geodetic studies show that north-central Chile lies within a highly coupled portion of the Chilean subduction zone between two small asperities at ~30°S and ~32°S (Fig. 1b; Métois et al., 2013). Three earthquakes with approximately similar along-strike rupture extents have occurred along the same portion of the subduction zone in 1880 (M ~7.7), 1943 (M_w 7.9), and 2015 (M_w 8.3; DeMets et al., 1994; Beck et al., 1998; Heinze, 2003; Saillard et al., 2009; Métois et al., 2013; Soto et al., 2014; Barnhart et al., 2016). However, the down-dip slip distributions of the 1880, 1943, and 2015 earthquakes likely differed (Tilmann et al., 2016). The relatively low (<4 m) and localized tsunami heights associated with the 1880 and 1943 earthquakes, respectively, suggest that they lacked sufficient shallow slip to produce a widespread tsunami. In contrast, the final rupture phase of the 2015 earthquake occurred on the shallowest part of the plate interface, resulting in relatively high (>4 m) and widespread tsunami heights in north-central Chile (Tilmann et al., 2016). Historical accounts indicate that tsunamis occurring in 1730 and 1922 CE were comparable in height to the 2015 tsunami and caused similar impacts to north-central Chile (Lomnitz, 1970); however, both previous earthquakes were centered largely on parts of the subduction zone either south of 32°S (1730, $M_w > 9$; Carvajal et al., 2017b) or north of 30°S (1922, M 8.5–8.6; Métois et al., 2013; Carvajal et al., 2017a; Kanamori et al., 2019) (Fig. 1c).

2.2. Pachingo marsh

We studied Pachingo marsh (30.3°S, 71.7°W) in southern Tongoy Bay, one of the few low-energy, organic-rich depositional environments in the region with the potential to preserve tsunami deposits (Fig. 2). The marsh is approximately 0.3 km^2, lies between about 0.5 and 1.0 m above modern mean sea level (MSL; all elevations that follow are relative to mean sea level), and is covered by a mono-dominant community of *Sacocornia fruticose*, a coastal plant typical of semi-arid to arid coastal environments (Muscolo et al., 2014). A ~75-m-wide beach bordered by a ~2.0-m-high berm separates the marsh from the bay. An unpaved road (0.69 m elevation) runs parallel to the shoreline at the transition between marsh and beach environments (Fig. 2c). In the western portion of the marsh, the ephemeral Pachingo River flows south to north. The river is sourced in the coastal range that lies ~30 km inland and dams in the western portion of Pachingo marsh forming a basin without an outflow to the bay (Fig. 3a; Soto et al., 2014). The pooling of the Pachingo River has allowed a low-energy marsh dominated by fine-grained sediment to form along a coastline otherwise dominated by high-energy sandy environments.

A series of Pleistocene and Holocene marine terraces and beach ridges characterize the landscape surrounding Pachingo marsh. They partially record the complex interaction of past sea-level highstands and long-term tectonic uplift over the last 700,000 years (Ota and Paskoff, 1993; Saillard et al., 2009; Soto et al., 2014). The most recent marine terrace lies at 2.7 m and was formed during the mid-Holocene sea-level highstand that occurred in the region ~6000 cal yr BP (Ota and Paskoff, 1993; Garrett et al., 2020).

Previous studies conducted near Pachingo marsh show that the area was likely a shallow intertidal environment for thousands of years following the highstand, when sea level was over 2 m higher at the site, and has undergone significant environmental changes due to long-term tectonic uplift and sea-level fall during the late Holocene (Ota and Paskoff, 1993). At a coring site ~50 m east of Pachingo marsh (site location on Fig. 2a), May et al. (2013) report geochemical evidence of marine mollusks in a basal sand dated to ~1000 cal yr BP, followed by a gradual decrease in marine influence at the site. Additional radiocarbon ages from the most seaward beach ridge east of our coring site (Ota and Paskoff, 1993) suggest that there was a seaward shift of the shoreline of ~100 m after 500 cal yr BP. This shoreline shift restricted the flow of the ephemeral Pachingo River and initiated the formation of a brackish, back-barrier environment which gradually evolved into the stable, low-energy freshwater environment found at Pachingo marsh today (May et al., 2013).

The modern climate in north-central Chile is semi-arid (<70 mm of rainfall per year) and characterized by prolonged multi-year droughts or extremely rainy seasons, which can cause flooding and debris flows in rivers and ephemeral streams (Pfeiffer et al., 2011). Tongoy Bay is wave-dominated and microtidal with a mixed semidiurnal regime and a maximum tidal range of about 1.8 m during spring tides (tidal range of 1.12 m between MLLW-MHHW) as measured by the Chilean Hydrographic and Oceanographic service (SHOA) at a tide gauge installed in 2018 at Puerto Aldea (~4 km west of Pachingo; Fig. 2a).

The wave climate offshore of Tongoy Bay is mainly controlled by austral winter swells emerging from extratropical cyclones, which propagate from the South Pacific Ocean towards the Chilean coast (Beyá et al., 2016, 2017). However, due to the northward-facing orientation of Tongoy Bay and the natural shelter provided by the Punta Lengua de Vaca peninsula to the west (Fig. 2a), waves approaching the bay from the south experience strong diffraction resulting in lower than average wave heights (Beyá et al., 2016,

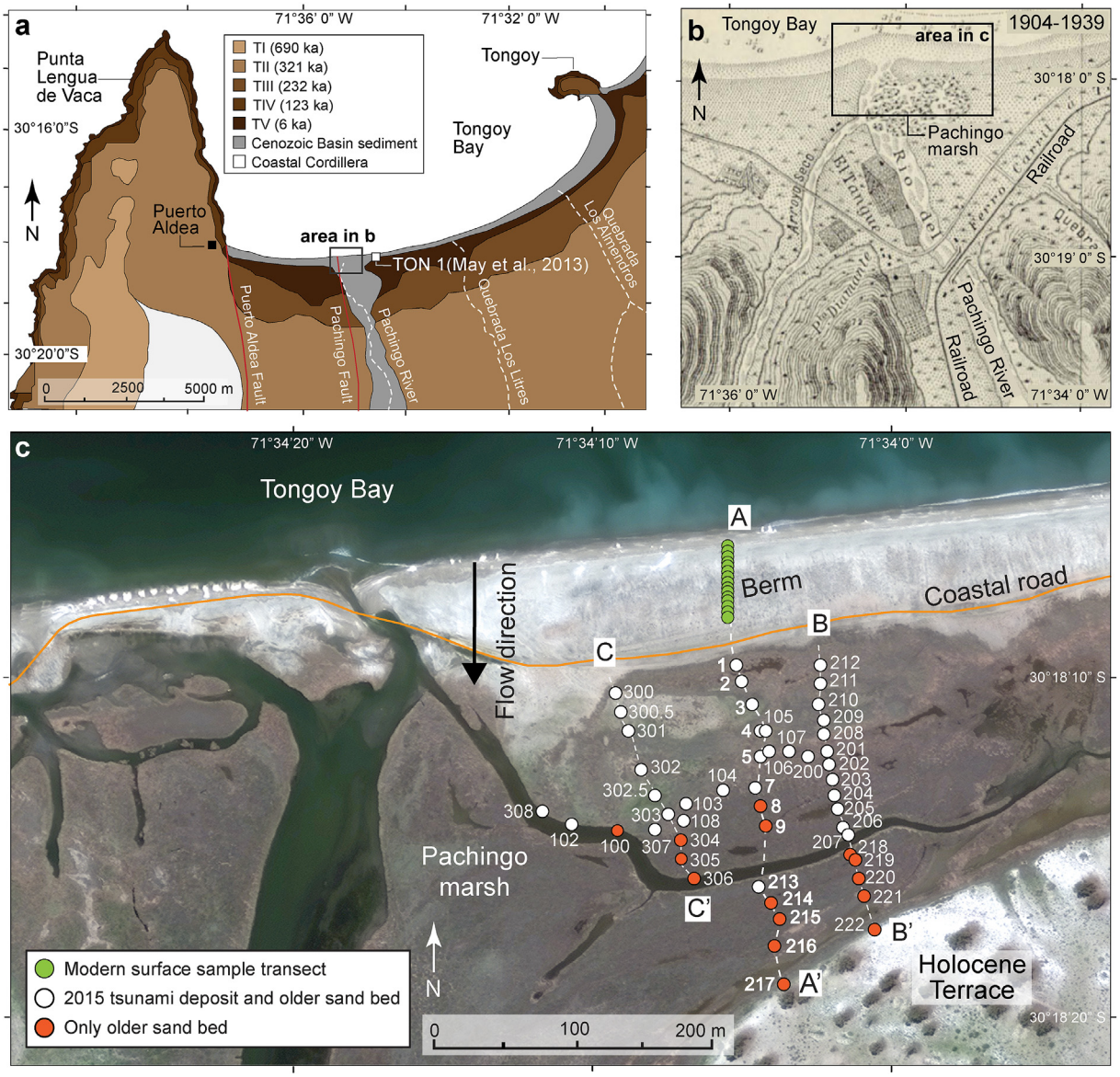

Fig. 2. a) Tongoy Bay and the Pachingo marsh located in north-central Chile <50 km south of the coastal town of Coquimbo. The marsh is bordered by Pleistocene-Holocene aged marine terraces (TV: 6 ka; TIV: 123 ka; TIII: 232 ka; TII: 321 ka; TI: 690 ka; Ota and Paskoff, 1993; Saillard et al., 2009, May et al., 2013). The tide gauge was located in Puerto Aldea (black square), b) Map of the Pachingo marsh from 1904 to 1939 CE (map source: Carta N° 53, Departamento de Navegación). The actual field site with sample locations (as shown in c) is marked by a black box. c) Satellite Google Earth Pro, 2014 Digital Globe imagery of the Pachingo marsh. The coastal road is highlighted with an orange line. Described and sampled locations were made in three transects (A-A′, B–B′, C–C′) perpendicular to the coast, shown by white dashed lines. Green circles are indicating where modern beach sediments were sampled along the A-A′ transect. Sample locations are labeled where the 2015 sand deposit and older sand bed are present (white circles) and where only the older sand bed is present (red circles).

2017). Swells arriving at Tongoy Bay from the north during the austral summer (between December and February) are usually associated with lower wave heights (Beyá et al., 2016, 2017). One of the largest coastal storms to strike north-central Chile in recent times occurred on August 8, 2015, when a combination of large wind waves (up to 7.2 m measured at a buoy off the coast of Valparaíso (33°S); Winckler et al., 2017), meteotsunamis (i.e. atmospherically induced tsunami-like waves), strong winds (110 km/h), and atmospherically-driven storm surges produced extreme flooding and coastal erosion along ~500 km of coast between Coquimbo and Bucalemu (34.5°S; Bahlburg et al., 2018; Carvajal et al., 2017c). A comparison of the satellite imagery of Pachingo marsh prior to the August 2015 extreme storm (Fig. 3a), shortly after the storm but before the September 2015 tsunami (Fig. 3b), and after the September 2015 tsunami (Fig. 3c, S3) shows that the storm caused minimal coastal erosion and no inundation or sediment deposition into Pachingo marsh.

2.3. Effects of the September 16, 2015 tsunami at Pachingo marsh

The largest instrumentally observed amplitude during the 2015 tsunami was recorded by the tide gauge closest to Pachingo marsh (Coquimbo, ~45 km to the north) with three tsunami waves reaching over 4 m and subsequent waves reaching 2 m throughout a full tidal cycle (Contreras-Lopez et al., 2016). According to Barnhart et al. (2016), the coastline along Pachingo marsh experienced vertical displacement of 5–10 cm. At our coring sites in the eastern part of Pachingo marsh, tsunami heights of up to ~3.5 m and

Fig. 3. Satellite Google Earth Pro, 2014 DigitalGlobe imagery of (a) Pachingo marsh on September 2014, (b) after the August 2015 large storm surge, and (c) after the September 2015 tsunami. A photograph of the browned vegetation from can be found in the supplementary materials (Fig. S3).

an inland inundation extent of >300 m were measured by Contreras-Lopez et al. (2016). Satellite imagery shows significant erosion at the mouth of the Pachingo River following the tsunami; enough sediment was removed to connect the river and Tongoy Bay for ~3–4 months before the coast recovered (Fig. 3). The imagery also shows erosion and inundation of the beach and road bordering

the eastern part of Pachingo marsh and sediment deposition and browned vegetation within the marsh (Figs. 4 and S3).

3. Approach and methods

To reconstruct the history of tsunami inundation at Pachingo marsh, we sampled 49 pit and gouge core locations along three coast-perpendicular transects (A-A′, B–B′, C–C′; Fig. 2c). We focused the bulk of our field descriptions and laboratory analysis on transect A-A′, which extends ~400 m inland from the shoreline and consists of 13 pits and cores spaced ~10–20 m apart (Fig. 2c). In the field, we described stratigraphy including color (Munsell soil color charts, 1975), sharpness of upper and lower contacts, and lithology and organic content using the Troels-Smith method for describing sediment (Nelson et al., 2015; Troels-Smith, 1955). We determined the locations and relative elevations of pits and cores using a differential GPS (Trimble, model R8). Elevations were then tied to our estimate of MSL at Puerto Aldea, determined by a portable acoustic tide gauge. Our estimate was then tied to the SHOA tide gauge that was installed later in 2018 at Puerto Aldea (Fig. 2a). Due to the relatively short period of recording of our tide gauge, we estimate an uncertainty of ±8 cm in the tie between our measurements and the MSL determined by the SHOA tide gauge.

3.1. Grain size analysis

To characterize the grain size distributions of the 2015 tsunami sediment and older sediment at the site, we conducted high-resolution (i.e., 1-cm) grain size analysis on locations representative of site stratigraphy (locations 2, 5, and 9 along transect A-A′; Figs. 2c and 5a). We also conducted bulk grain size analysis on anomalous sand beds from all other locations along transects A-A′, B–B′, and C–C′. To evaluate a potential source of tsunami sediment, we collected surface sediment samples (top 2 cm) along a coast-perpendicular beach transect adjacent to Pachingo marsh (Fig. 2c). Using pre-tsunami imagery, we targeted parts of the beach where tsunami erosion appeared minimal and collected 15 surface samples that spanned the intertidal to supratidal zone.

We treated sediment samples with hydrogen peroxide (30% concentration) to remove organic material. Using a Malvern Mastersizer 3000 laser-particle size analyzer we performed grain size analysis on the remaining inorganic material for each grain size sample (Donato et al., 2009). We calculated sample statistics using the GRADISTAT statistical software package using the Wentworth phi scale (Blott and Pye, 2001). We used mean grain size, sorting, skewness, D10 (the diameter where 10% of the sample volume is composed of smaller grains than the reported particle size), and D90 (the diameter where 90% of the sample volume is composed of smaller grains than the reported particle size) to characterize modern beach sediment and pit and gouge core sediment.

3.2. PAM cluster analysis

Partitioning Around a Medoid (PAM) cluster analysis (Kaufman and Rousseeuw, 1990) was used to resolve whether the older sand bed is more similar to the 2015 tsunami sediment or the basal sand in Pit 2 (Fig. 6). Grain size data (percent abundance per size category) were first used to calculate z-scores as a way of standardizing the dataset through assessing the number of standard deviations a value is from the mean. PAM cluster analysis was then performed using the cluster package in R (Maechler et al., 2005) following Kemp et al. (2012) and Pilarczyk et al. (2016). PAM cluster analysis generates silhouette plots that range in width from −1 (perfectly incorrect assignment to a particular cluster) to 1 (perfect assignment to an appropriate cluster). We used a three-cluster scenario representing the three main stratigraphic units (2015 tsunami sediment, organic silt, and basal sand) to test which unit the older sand bed is most similar to.

3.3. Dating

To constrain the age of the older sand bed, we used Cesium (^{137}Cs) and Lead (^{210}Pb) dating methods. Subsamples for the analysis were taken at 1-cm intervals throughout a monolith representative of site stratigraphy from location 5 (Fig. 7). The dating methods used to constrain the ages of the sand deposits were also used to calculate a sedimentation rate for Pachingo marsh. The sand beds were not used in the rate calculation because they likely represent an instantaneous influx of sediment rather than an accumulation over time.

As a byproduct of fission reactions, ^{137}Cs ($t_{1/2}$ = 30.1 years) is a dateable anthropogenic radionuclide produced by hydrogen bomb

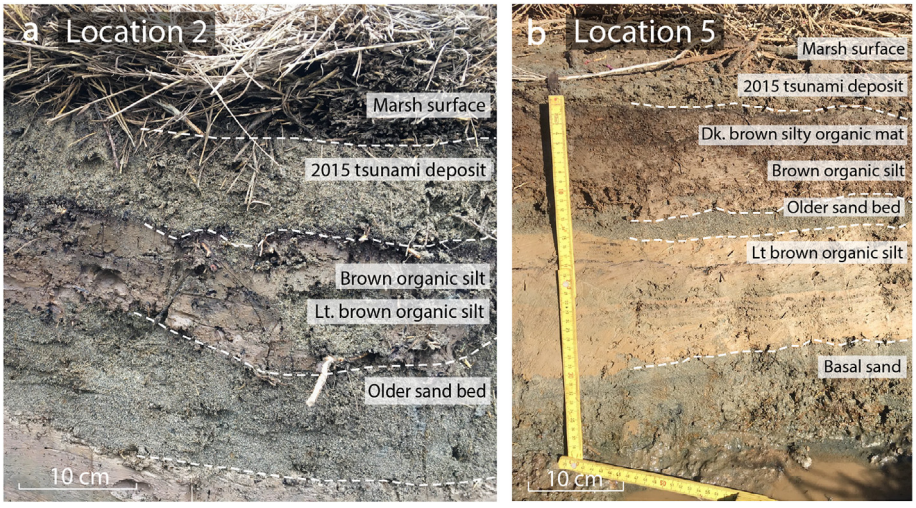

Fig. 4. a) Photograph of sediments at location 2 along transect A-A′ with stratigraphy labeled. Unit contacts are outlined in dashed white lines. Dense *Sacocornia* sp. roots and stems are found at the top of the stratigraphy labeled "Marsh surface", b.) Photograph of sediments at location 5 along transect A-A′ in Pachingo marsh with stratigraphy labeled. Unit contacts are outlined in dashed white lines. Dense *Sacocornia* sp. roots and stems can be seen at the surface.

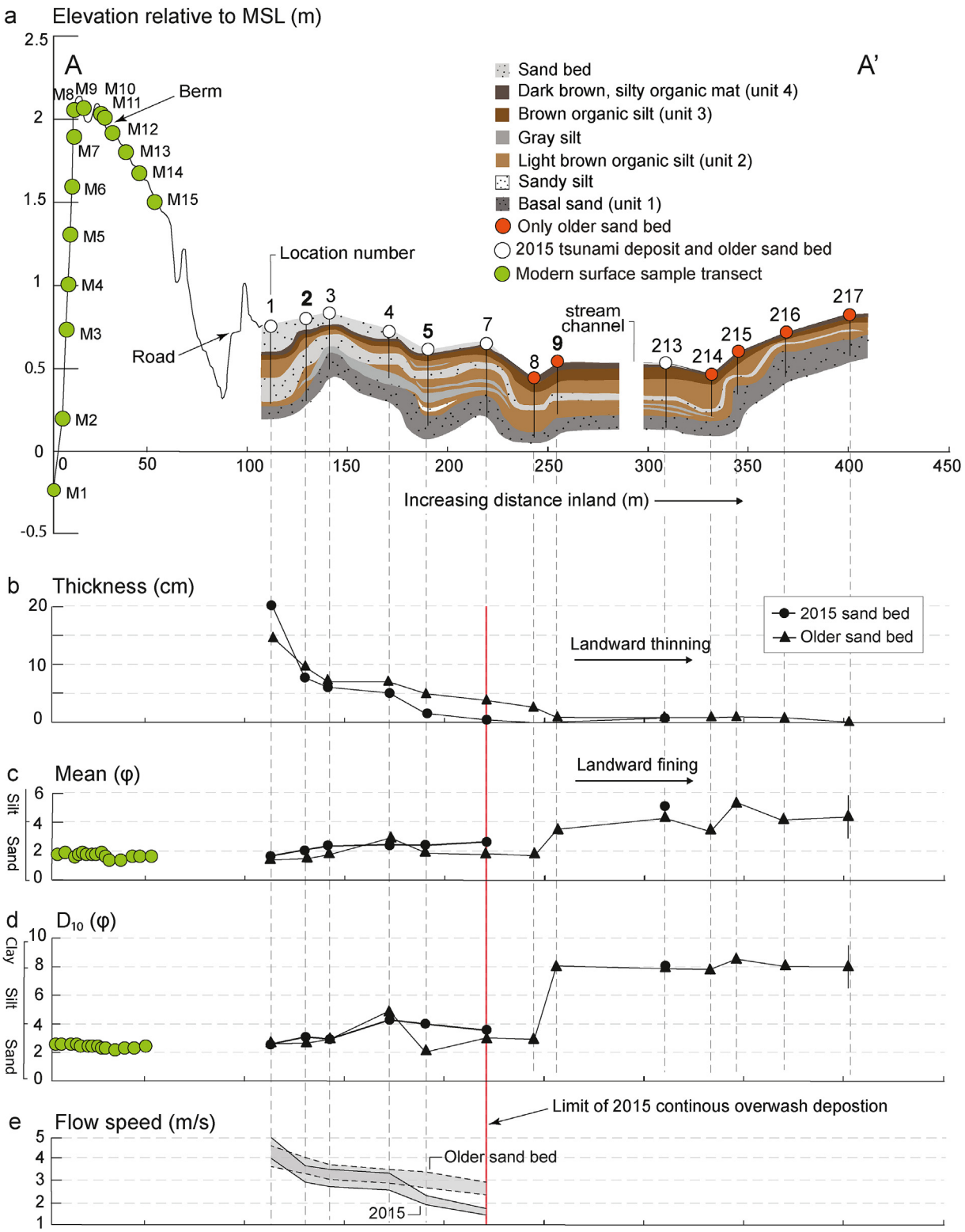

Fig. 5. a) Coast perpendicular elevation profile along transect A-A′ (see Fig. 2c for profile location) with detail of the Pachingo marsh stratigraphy. Sample locations along the transect are labeled and locations chosen for detailed analysis (2, 5, and 9) are in bold. Locations where the 2015 tsunami deposit and the older sand bed are present in stratigraphy (white circles) and locations where only the older sand bed is present (red circles) are marked. Modern sediment surface samples are shown with green circles (Ml-Ml5). The beach berm and coastal road are labeled. Elevations are relative to mean sea level (MSL). b) Thickness of deposit (cm), c) mean grain size (in phi; greater phi value = smaller grain size), and d) D10 (diameter at which 10% of a the sample volume is composed of smaller grains; in phi) are plotted for both the 2015 sand bed (solid line with circles) and older sand bed (dashed line with triangles). The red, solid, vertical line depicts the inland extent of the 2015 tsunami continuous deposition, e) Flow speed results using locations 1, 2, 3, 4, 5, and 7 from transect A-A′ are plotted for both the 2015 tsunami deposit (solid line) and the older sand bed (dashed line). The gray envelope represents the uncertainty of the flow speed values at each location.

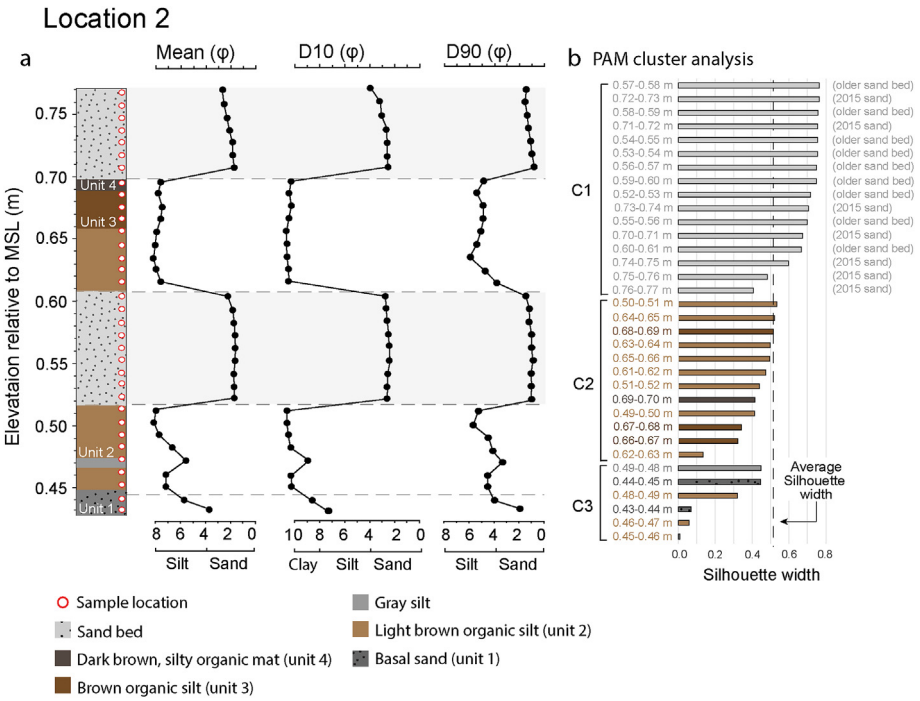

Fig. 6. a) Stratigraphic column at location 2 depicting sedimentary units. White circles with red outlines indicate where samples were taken for high-resolution grain size. Plots show values of mean grain size, D10 (diameter at which 10% of a sample's mass is comprised of smaller grains), and D90 (diameter at which 90% of a sample's mass is comprised of smaller grains). The 2015 tsunami deposit and older sand bed are shaded with light gray, b) PAM results show the stratigraphic layers with similar grain-size sorting in three clustering groups (CI, C2, and C3). The average silhouette width is 0.51.

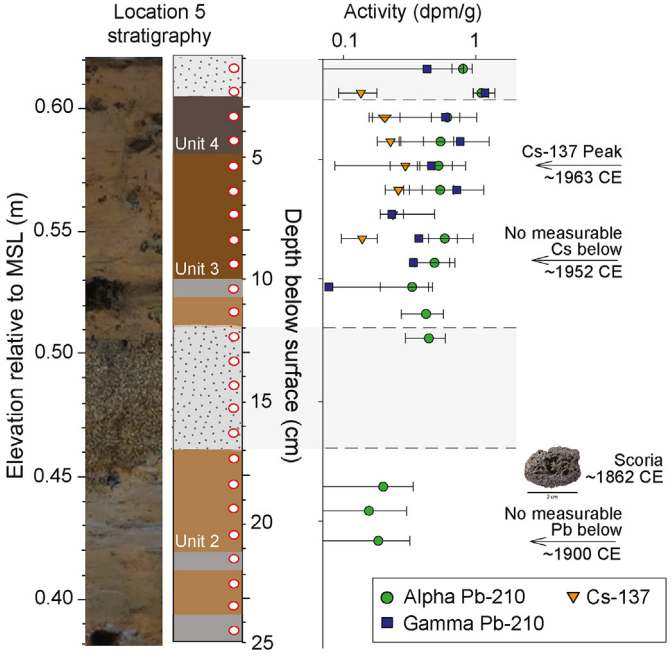

Fig. 7. Photograph of sediment monolith from location 5 used for geochronology, stratigraphic column of sedimentary units, and down-core activity (dpm/g) of excess ^{210}Pb (green circles - alpha; blue squares - gamma) and ^{137}Cs (orange triangles). Lithologies are explained in Figure 5. The down-core peak of ^{137}Cs (corresponding to ~1963 CE) and depth of no measurable ^{137}Cs (corresponding to ~1952 CE) are indicated by arrows. Additionally, an arrow pointing to the depth of no measurable excess ^{210}Pb data (below ~0.42 m MSL) indicates the year ~1900 CE. Pieces of scoria, which may be debris from a railroad bed dating back to ~1862 CE, were found just below, within, and above the older sand bed. The depth ranges of the 2015 tsunami deposit and older sand bed are shaded with light gray.

testing and deposited across the globe beginning November 1952 and peaking in 1963. The ^{137}Cs is significantly less detectable in the southern hemisphere due to reduced hydrogen bomb testing activities, but this method can be used to date sediment deposited ~60 years ago (Corbett and Walsh, 2015). Following Corbett and Walsh (2015), we use 1950 as the onset of ^{137}Cs and 1963 as the peak in ^{137}Cs in our sedimentation rate calculations.

As a naturally occurring radioisotope, ^{210}Pb ($t_{1/2} = 22.3$ years) is a product of the Uranium-238 decay series and is continually being produced in the atmosphere and on Earth's surface (Corbett and Walsh, 2015). Lead-210 is a useful tracer for dating sediment up to ~110 years old (or approximately five half-lives). ^{210}Pb, ^{226}Ra (e.g., supported ^{210}Pb), and ^{137}Cs activities were determined by gamma spectroscopy on a low-background, high-efficiency, high-purity Germanium detector. Samples were initially dried, homogenized by grinding, packed into standardized vessels, and sealed before counting for at least 24 h. Activities were corrected for self-absorption using a direct transmission method (Cable et al., 2001). Excess ^{210}Pb activities were determined by subtracting total ^{210}Pb from that supported by ^{226}Ra, determined via ^{214}Pb and ^{214}Bi. Analysis of ^{210}Pb was also achieved by alpha spectroscopy following Nittrouer et al. (1979). The supported ^{210}Pb activity by this method was assumed to be equal to the uniform background activity found at depth.

To better understand the geomorphological evolution of the site over centuries, we examined historical maps of Pachingo marsh dating back to 1889 (SHOA chart N° 53). The maps provided a means to investigate the previous location of river channels, beach width, and land use history at Pachingo marsh, allowing us to put previous potential inundation of the marsh by tsunamis into context of historical shoreline change.

3.4. Geochemical analysis

To understand the environmental changes that have occurred at Pachingo marsh over the last few centuries and investigate the potential for coseismic land-level change at the site, we analyzed the total organic carbon (TOC) content, the ratio of organic carbon to total nitrogen (C:N), and stable carbon isotope (^{13}C) composition of the organic matter in a core from location 9 (Fig. 8). Variations in these parameters can be used to track the sources of organic matter at Pachingo marsh (reviewed by Woodroffe et al., 2010 and Khan et al., 2015). At Pachingo marsh, we predict that lower wt% TOC and C:N ratios (5–10) would reflect a greater contribution of organic matter, while higher wt% TOC and C:N ratios (>15) would reflect a greater contribution of terrestrial and/or freshwater derived organic matter. More negative ^{13}C would reflect more organic matter from terrestrial C3 plants and freshwater algae (^{13}C values −28 to −22‰), while less negative values would indicate a greater contribution from terrestrial C4 plants (^{13}C values −17 to −9‰) or marine organic matter (−25 to −18‰). C3 and C4 plants utilize the C3 and C4 photosynthetic pathways, respectively. Today the vegetation of Pachingo marsh is dominated by *Sarcocornia fruticose*, a halophytic C3 plant that accounts for more than 95% of the ground cover (Fariña et al., 2018).

We subsampled a core from location 9 (Fig. 8) at 2-cm intervals in homogenous sediment and at 1-cm intervals 5 cm above and below the older sand bed. From each subsampling location we transferred ~3 cm^3 of sediment to a 50 mL centrifuge vial and followed the methods of Woodroffe et al. (2010) to measure TOC, C:N, and ^{13}C.

Samples were analyzed using an Elementar vario isotope elemental analyzer coupled to an Isoprime 100 continuous flow isotope ratio mass spectrometer in the Department of Geoscience at Virginia Tech. Stable carbon isotopic compositions were calibrated relative to the VPDB scale using the international standards IAEA CH-6 (−10.449‰) and IAEA CH-7 (−32.151‰) and a commercial standard Elemental Microanalysis wheat flour (−27.21‰). Precision for the $\delta^{13}C$ measurements was determined to be within ±0.1‰ (1σ) based on replicate measurements of calibration standards and samples. Total nitrogen and organic carbon contents of each sample were determined using the area of the N_2 and CO_2 peaks measured by the elemental analyzer calibrated to size series of acetanilide elemental standards. The nitrogen and carbon contents of acetanilide and wheat flour standards, spaced throughout the analytical runs and not used in the calibration, were within 5% from their reported contents. Precision of the nitrogen and carbon elemental analyses was determined to be better than 0.1% and 0.2% wt% (1σ), respectively, based on replicate measurements of calibration standards and samples.

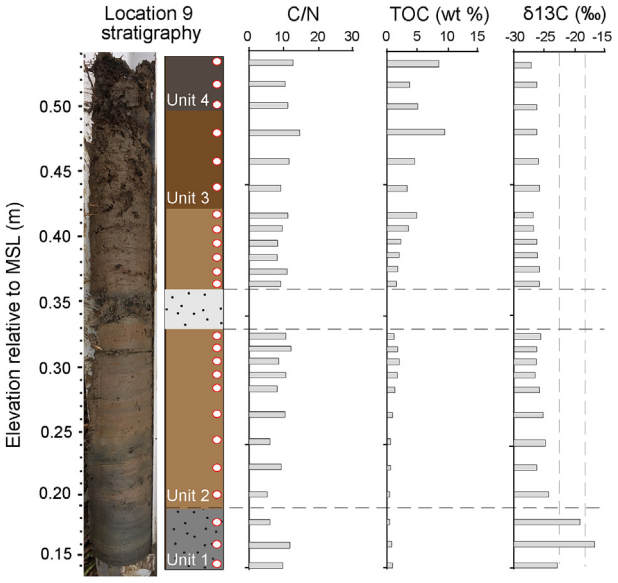

Fig. 8. Photograph of the core from location 9 used for geochemical analysis, stratigraphic column of units from location 9, organic carbon to total nitrogen ratio (C/N) plot, total organic carbon (TOC) plot, and ^{13}C plot Lithologies explained in Fig. 5.

3.5. Tsunami flow inversion

To understand the flow characteristics of the 2015 tsunami at our site and compare them to potential tsunami-flow conditions that affected the site in the past, we used the TSUnami FLow INversion from Deposits model (TSUFLIND from Tang and Weiss, 2015, Fig. 5e). TSUFLIND is a model that takes field and laboratory observations of a known or inferred tsunami deposit as input to estimate the flow speed, offshore wave amplitude, Froude number, and flow depth of the tsunami that created the deposit (Tang and Weiss, 2015). We focused on the flow speed output of TSUFLIND to compare the relative size of the 2015 tsunami with the older tsunami candidate identified at the site.

Inputs to the model include grain size, topographic data, and deposit thicknesses from both sand beds at sampling locations along transect A-A′ (Tang and Weiss, 2015). We considered several assumptions that the TSUFLIND program requires: 1) the sediment must be deposited from suspended load (evidence of upward fining of sediment must be present), 2) there is a pattern of landward fining of the sediment, and 3) the topography of the study site does not have significant relief (Tang and Weiss, 2015).

The 2015 deposit and the older sand bed satisfied the assumptions of the model, which allowed us to run TSUFLIND for both sand beds independently. We used locations 1, 2, 3, 4, 5, and 7 for modeling because locations inland of 7 varied too greatly in elevation (Fig. 5a, c).

3.6. Tidal modeling

In order to investigate the influence of the tidal stage on tsunami inundation heights at the time of past tsunami arrivals, we estimated the tide levels during four candidate historical tsunamis that may have deposited the older sand bed at our site (1730, 1880, 1922, and 1943; Fig. S7). We first searched and analyzed published literature and historical documents to estimate the UTC time of the historical earthquakes that generated tsunamis. Then, we reconstructed the historical tide levels during each earthquake by applying a harmonic analysis to recorded, modern sea level data using the T-Tide MATLAB toolbox (Fig. S7; Pawlowicz et al., 2002). The recorded sea level data was one-year-long and spanned from July 2018 to July 2019 at the Puerto Aldea tide gauge. In particular, we used T-Tide to extract the amplitudes and phases of the major harmonic constituents recorded from the data and then used them to reconstruct the tide levels at the time and date of the candidate historical tsunamis (Fig. S7). We validated the tidal model by comparing modeled tidal time series with available tidal records on other temporal windows.

4. Results

4.1. Site stratigraphy

We observed four main lithostratigraphic units (units 1, 2, 3, 4)

and two distinct, anomalous sand beds in the Pachingo marsh stratigraphy (Figs. 5a and 6, S1-S2; grain size results for locations 5 and 9 can be found in the supplementary material). A compact, gray (5Y 5/1) very fine sand (unit 1; mean = 4.01 φ; D10 = 9.85 φ) containing very little organic material uniformly underlies the marsh sediment between 0.04 and 0.54 m. Exploratory cores and pits show that the basal sand extends well below 0.04 m. In seaward locations (e.g., locations 2 and 5), the basal sand contains large (>3 cm) whole, articulated shells as well as many fragments (<1 cm) of shells. A 0.10–0.15 m thick light brown (7.5 YR 5/4) silt (unit 2; mean = 7.31 φ; D10 = 10.00 φ) overlies the basal sand in most parts of the marsh. Unit 2 contains sparse humified organic matter. Beds of discontinuous gray (5Y 6/1) silt (<6 cm thick; mean = 5.62 φ; D10 = 9.21 φ) and gray (5Y 6/1) sandy silt (<2 cm thick; mean = 2.58 φ; D10 = 4.15 φ) are interbedded within the lower portions of unit 2 in some locations (Fig. 5a, S1). A 0.05–0.10 m thick, brown (7.5 YR 4/3) organic silt (unit 3; mean = 7.45 φ; D10 = 9.89 φ) overlies unit 2. It is distinguished from unit 2 by its darker color and the presence of visible plant fragments and roots (5–10 mm long). A 0.01–0.04 m thick, dark-brown (7.5 YR 3/2), rooted, silty organic mat (unit 4; mean = 7.35 φ; D10 = 9.85 φ) is found consistently at all locations along transect A-A′ above the brown organic silt (unit 3).

We mapped two distinct anomalous sand beds along transects A-A′, B–B′, and C–C′: the 2015 tsunami deposit and an older sand bed interbedded within unit 2 (Figs. 2c, 4 and 5, S1-S2). A laterally continuous sand bed deposited by the 2015 tsunami is found between 0.50 and 0.78 m and extends ~275 m inland (measured along transect B–B′) and ~275 m laterally (Fig. 2c). The sand bed varies in thickness from 20 to <1 cm, is composed of fine-to medium-grained, moderately sorted, micaceous, gray-brown (2.5Y 5/1) sand (mean = 2.07 φ; D10 = 1.30 φ), and thins and fines landwards. Grain size samples taken at 1 cm vertical intervals from the 2015 sand bed at locations 2 and 5 show upward fining and an increased fine fraction towards the top of the sand bed (Fig. S1, S2). The 2015 tsunami deposit flattened and buried the surface of Pachingo marsh, creating the distinctive dark-brown, rooted, silty organic mat (unit 4) described above.

An older sand bed interbedded within unit 2 is found between 0.28 and 0.73 m and extends ~400 m inland and ~250 m laterally (Figs. 2c and 5). The older sand bed varies in thickness from 15 to <1 cm, is composed of fine-to medium-grained, poor to moderately sorted, micaceous, gray-brown (2.5Y 5/1) sand (mean = 1.96 φ; D10 = 3.32 φ), and thins and fines landwards. Grain size samples taken at 1 cm vertical intervals from the older sand bed at locations 2, 5, and 9 show upward fining and an increased fine fraction towards the top of the sand bed (Fig. S1-S2).

Both sand beds are distinct from their under- and over-lying units due to their greater mean grain size, low organic content, characteristic sharp (1–3 mm) or eroded lower and upper contacts, and fining upwards grain size trends. Both sand beds thin and fine landwards and are laterally continuous over hundreds of meters. However, the older sand bed extends >125 m farther inland than the 2015 tsunami deposit (Figs. 2c and 6). PAM cluster analysis on Pit 2 sediment grouped 2015 tsunami sediment and the older sand bed together (Cluster 1; Fig. 7b) and grouped these sand beds separately from other units (average silhouette width = 0.51). Cluster 1 (C1; average silhouette width = 0.69) consisted entirely of 2015 sediment and those from the older sand bed. Cluster 2 (C2; average silhouette width = 0.42) consisted of organic silt layers from units 2 and 3; while Cluster 3 (C3; average silhouette width = 0.22) generally consisted of basal sand (unit 1) with a minor contribution of organic silt intervals from below the older sand bed.

Modern surface samples (M1–M15) collected from subtidal, beach, and beach ridge environments adjacent to Pachingo marsh were composed of gray (5Y 6/1) to gray-brown (2.5Y 5/1), poorly to moderately sorted, micaceous, fine-to medium-grained sand (mean = 1.70 φ; D10 = 1.02 φ), with the lowest elevation subtidal and beach samples containing a higher fine-sand component compared to higher elevation beach and beach berm samples (e.g., M1 sampling location D10 = 1.22 φ and M13 sampling location D10 = 0.67 φ; Fig. 4a, 4c-d).

4.2. Dating the older sand bed using ^{137}Cs, ^{210}Pb, scoria, and historical maps

Our ^{137}Cs and ^{210} Pb dating results constrain the timing of the deposition of the top 21 cm of sediment (between 0.42 and 0.62 m at location 5) in Pachingo marsh (Fig. 7). A peak of ^{137}Cs 5–6 cm below the surface (between 0.57 and 0.58 m) corresponds to a depositional age of ~1963 CE, while no ^{137}Cs present below 9 cm in the core (0.54 m) corresponds to the depositional age of 1952 CE. Assuming continuous sediment accumulation in the marsh, we calculate an average sedimentation rate of ~0.12 cm/yr between the near-surface marsh sediment and the peak in ^{137}Cs (~0.11 cm/yr) and between the near-surface sediment and the absence of ^{137}Cs in the core (~0.13 cm/yr). Based on this accumulation rate, the top 13 cm of sediment (between 0.42 and 0.62 m; excluding the thickness of the sand beds) was deposited in the last ~110 years (i.e., after 1910 CE). This is consistent with low-level ^{210}Pb alpha activity between 21 and 25 cm depth in core (between 0.38 and 0.42 m) suggesting that sediment above this depth was deposited after ~1900 CE. Assuming this sedimentation rate applies to the depth of the basal sand, we can constrain the age of the onset of back-barrier fine sediment deposition in the marsh to ~1800 CE (~220 years BP; Fig. 7).

To further constrain the timing of deposition of the older sand bed, we investigated 1–3 cm diameter scoria fragments found just below, within, and above the sand (Fig. 7). We tracked the source of the scoria to a railroad bed, depicted on historical maps, that was under construction starting in 1862 (Astaburuaga, 1899) and in operation by 1867 (Long, 1930). Historical maps show the railroad running south of the site and crossing the Pachingo River to a copper smelter waste site in northeast Tongoy Bay, which was in operation between 1839 and the late 1880s CE (Figs. 2b, S4, and S5; Long, 1930). We identified the old railroad bed with scattered railroad nails and scoria pieces where the historical maps depict the railroad. We infer that the scoria was used to support the railroad bed and was likely washed into the river or terrace adjacent to Pachingo marsh, and then transported into the marsh by infrequent, heavy, localized river flooding or tsunamis, providing an additional maximum age constraint of 1862 CE for the deposition of the upper ~20 cm of sediment.

Historical maps depicting Tongoy Bay and Pachingo marsh in 1889–1904 (Fig. S4) and 1904–1939 (Fig. S5) show a marsh similar to that of today for at least the last ~130 years. The older map shows Pachingo marsh covering a similar area to the modern marsh extent, however, the Pachingo River is connected to Tongoy Bay, suggesting that the fluvial geomorphology and influence of coastal water was different at that time. The main river channel is in about the same position, suggesting it has not migrated recently; however tributaries are shown on the map that are not present in the modern marsh. This observation suggests that the marsh has been influenced by fluvial channel migration, which may have deposited some of the discontinuous coarse silt and fine sand layers that we observed in locations 2, 3, 4, 5, 7, and 213 (Fig. 2c). The map from 1904 to 1939 shows a very similar geomorphology to that of today. The river, like today, does not connect to Tongoy Bay, but instead

pools at its terminus (Figs. 2b, S5). Using our ^{137}Cs and ^{210} Pb dating results and historical analyses, we conclude that the environment and geomorphology of Pachingo marsh was not significantly different when the older sand bed was deposited (Figs. S4-S6).

4.3. Geochemical analysis

Samples from the basal sand at location 9 (~0.19 m) exhibit low organic content (TOC = 0.56 wt%), low C:N values (~6.6 and 12.3), and ^{13}C enrichment (~-17.4 and −19.0‰; Fig. 7) consistent with a more significant marine influence at the site. Starting ~5 cm below the older sand (~0.28 m) there is a gradual increase in TOC (from <1% to >5 wt%) and a gradual fall in ^{13}C values (~-25‰). Over the same interval, C:N values are variable but are generally higher and average ~10. Overall these patterns likely reflect an increase in the terrestrial/freshwater contribution to the organic matter at the site.

Between ~0.48 m and ~0.51 m (units 3 and 4), the highest TOC (5–10 wt%) and C:N values (~12) and the lowest ^{13}C values (~-27‰) are recorded in the core reflecting the current terrestrial/freshwater environment at the site today. Notably, the carbon isotope compositions of the organic material in the uppermost portion of the core agree with what would be expected from the dominant vegetation in Pachingo marsh today: the ^{13}C of *Sacocornia fruticosa* found elsewhere has been reported as −28.5‰ to −26.0‰ (França et al., 2011; Vinagre et al., 2008). We also note there are no major shifts in TOC, C:N, or ^{13}C values across the older sand bed suggesting there were no distinct environmental changes before and after sand deposition.

4.4. Tsunami flow inversion

4.4.1. Flow speeds for the 2015 tsunami deposit

Model output for the 2015 tsunami deposit shows a decrease in flow speed as it moved inland from location 1 (110 m inland) to 7 (221 m inland; Fig. 5e). Model-reconstructed flow speeds were initially between 3.98 and 5.07 m/s at location 1 and incrementally decreased inland due to the interaction with marsh vegetation and loss of momentum. As the flow reached location 4 (171 m inland) it had already slowed to between 2.63 and 3.31 m/s. By the time the tsunami inundation reached location 7 it was moving between 1.40 and 1.74 m/s, nearly three times slower than its original speed.

4.4.2. Flow speeds for the older sand bed

Model output for the older sand bed also shows a decrease in the tsunami flow speed as it moves inland from location 1 to 7. Speeds were calculated to be between 3.61 and 4.59 m/s at location 1, gradually losing momentum and slowing to between 2.83 and 3.52 m/s at location 4. When the tsunami inundation reached location 7, it had only slowed to between 2.30 and 2.88 m/s, ~1 m/s faster than the speed calculated at location 7 for the 2015 tsunami. With the exception of location 1, all flow speeds calculated for the older sand bed are faster than the speeds for the 2015 tsunami, providing a relative comparison in the strength and size of the tsunamis that deposited these sand beds.

5. Discussion

5.1. The environmental evolution of Pachingo marsh over the last two centuries

Based on our field observations, laboratory analyses, and historical investigation we reconstruct the depositional environments represented by the lithologic units at Pachingo marsh and identify instances of anomalous marine incursions into the site in the last two centuries. At the base of our seaward sampling locations, we observed fragmented and whole articulated shells in the basal sand that are characteristic of shallow intertidal or open marine environments. This is consistent with our geochemical results that indicate marine conditions prevailing at the base of location 9, as shown by the low organic content (TOC), low C:N values, and ^{13}C enrichment of the basal sediment. A gradual transition to lower energy, brackish conditions is reflected by the deposition of finer-grained material with a higher organic content, a gradual rise in TOC and C:N values, and a gradual fall in ^{13}C values starting ~5 cm below the older sand bed. This gradual transition continues until maximum TOC and C:N values and minimum ^{13}C values are observed in the top ~5 cm of location 9, reflecting the current freshwater environment of Pachingo marsh.

The timing of the transition from shallow intertidal conditions at the base of our locations to a stable, freshwater low-energy depositional environment is constrained by our ^{137}Cs and ^{210}Pb dating, historical maps, and previous studies in the area. Based on sediment accumulation rates (0.12 cm/yr; Fig. 7) calculated from the presence of ^{210}Pb (~1900 CE), the appearance of ^{137}Cs (~1952 CE), and the ^{137}Cs peak (~1963 CE) from our core at location 5, we infer that the onset of back-barrier conditions at the base of our sections occurred ~220 years ago. Our results are supported by historical maps showing similar marsh morphology at Pachingo in 1889 CE and previous studies that constrained the timing of a recent ~100 m seaward shift of the shoreline at Pachingo to sometime after ~500 years (Ota and Paskoff, 1993) and ~1000 years (May et al., 2013) ago.

We infer that the seaward shift and progradation of the shoreline over the last ~220 years occurred due to relative sea-level fall following the mid-Holocene sea-level highstand (Dura et al., 2015; Garrett et al., 2020), probably with slow tectonic uplift of the coast (Ota and Paskoff, 1993; Saillard et al., 2009). It has also been suggested that periodic punctuated uplift along the coast during earthquakes in the late Holocene may have contributed to the seaward shift of the shoreline (May et al., 2013). However, we do not find evidence of sudden coastal uplift in Pachingo marsh stratigraphy; the geochemical changes we observe are gradual and not associated with sand bed deposition, suggesting that they are not driven by coseismic deformation.

5.2. Evidence for tsunami inundation

Based on our field observations, the 2015 tsunami deposit was still visible in sample locations across the study site three years after the tsunami. It had already been buried in some other locations, which increases the likelihood of long-term preservation. Thus, the 2015 sand bed is a good modern analog for tsunami inundation and deposition at Pachingo marsh.

Based on the similarities observed in the spatial extent and grain size characteristics of the 2015 tsunami deposit and the older sand bed, we infer a tsunami origin for the older sand bed (Table 1, Table S1). PAM cluster analysis corroborates this interpretation by clustering older sand bed samples with 2015 tsunami samples in cluster 1 (C1), where a relatively high silhouette width (0.69) indicates strong similarity between both units (Fig. 6). Other sand (e.g., the basal sand) or silty sand (e.g., inferred fluvial sediment) layers within the stratigraphy clustered separately, suggesting either a difference in provenance or mechanism of deposition. The 2015 sand bed and older sand bed are both composed of gray, medium-to fine-grained sand similar to the sand found in the seaward beach (Fig. 5c and d), consistent with a landward marine incursion eroding, transporting, and depositing sediment onto the marsh. Both sand beds display sharp, erosive lower and upper contacts, are laterally continuous over hundreds of meters, thin and fine landward, and fine upward (Fig. 5, Table 1). Similar physical

Table 1
Comparison of sedimentary, stratigraphic, and modeled characteristics between the 2015 tsunami deposit and the older sand bed.

	2015 tsunami deposit	Older sand bed
Tsunami criteria		
Laterally continuous deposit (inundation >200 m inland)	X	X
Upward fining	X	X
Landward fining	X	X
Landward thinning	X	X
Sharp or erosive lower contact (<1–3 mm)	X	X
Similar in composition to modern samples	X	X
Sand bed characteristics		
Coarsest grain size (phi)	1.8	1.7
Inland extent of overwash sediment (m)	~275	~400
Maximum bed thickness (cm)	20	14
Flow speed at location 1 (m/s)	3.98 to 5.07	3.61 to 4.59
Flow speed at location 7 (m/s)	1.40 to 1.74	2.30 to 2.88

and spatial characteristics have been reported from modern tsunami deposits described elsewhere in Chile (e.g., Cisternas et al., 2005; Horton et al., 2011; Garrett et al., 2013; Ely et al., 2014; Dura et al., 2015), Thailand (e.g., Jankaew et al., 2008; Sawai et al., 2008), Sumatra (e.g., Kelsey et al., 2015), and Japan (Goto et al., 2011).

We consider the possibility that the older sand bed was deposited by a coastal storm, as previous studies have noted the similarities between tsunami and storm deposits (Morton et al., 2007; Tuttle et al., 2004). Although we cannot rule out the possibility of a coastal storm depositing the older sand bed, we believe a tsunami is a more likely source for several reasons. First, as pointed out in Section 2.2, the largest coastal storm in recent times, occurring on August 8, 2015 (Winckler et al., 2017), did not inundate Pachingo marsh (Fig. 3). Based on historical maps that indicate the geomorphology of the marsh has not significantly changed in the last ~130 years (Fig. S4-S6), we infer that sand deposition by a storm during the time period when the older sand bed was deposited (last ~110 years), is unlikely. Second, the 2015 storm, despite causing severe damage to coastal infrastructure in other places along the central Chile coast, only affected a narrow band along the coastline. Third, Pachingo marsh is naturally protected from most coastal storms approaching from the southwest or west due to the north-south trending Punta Lengua de Vaca peninsula bordering the western side of Tongoy Bay (Fig. 2a). And finally, because tsunamis triggered by subduction zone earthquakes have much longer wave periods (10^2–10^3 s), they are expected to reach much further inland, than shorter-period waves (<10^2 s) associated with storms (Fujiwara and Kamataki, 2007).

We infer that the discontinuous, thin, coarse silt and fine-grained sand deposits found below and just above the older sand bed in the stratigraphy at locations 2, 3, 4, 5, 7, and 213 were produced by river floods and/or river channel migration at the site. These relatively thin (<6 cm thick) deposits are similar in composition to sediment observed in the current Pachingo River channel and lack the spatial and grain size characteristics of the 2015 tsunami deposit and older sand bed. Furthermore, as noted above, PAM cluster analysis does not cluster these coarse silt and fine-grained sand deposits with our inferred tsunami sand beds (Fig. 6), and therefore indicates a difference in provenance or mechanism of deposition for these finer sediments.

5.3. Relative size of the tsunamis that inundated Pachingo marsh

To determine the relative size and inland extent of the flow that deposited the sand beds preserved in Pachingo marsh, we used field, laboratory, and modeling results to compare sand bed characteristics. Field and laboratory observations show that the older sand bed is thicker on average, extends further inland, and is coarser than the 2015 tsunami deposit (Table 1, Table S1). Because our historical and dating analyses suggest similar site conditions within the past ~110 years when the older sand bed was deposited, we infer that the older sand bed was deposited by a higher and faster flow than the 2015 tsunami at Pachingo marsh.

Our tsunami flow inversion modeling supports our interpretation that the older sand bed was deposited by a faster tsunami flow at this site (Fig. 5e). Model results show that the flow that produced the 2015 deposit and older sand bed had faster speeds near the coast and slowed as they progressed inland. This characteristic is typical of tsunami flow and is the principal process for depositing sediment out of suspension. However, with the exception of location 1, the flow speeds associated with the deposition of the older sand bed were faster at all sampling locations than the flow speeds calculated for the 2015 tsunami deposit (Fig. 5e), supporting our inference that the older sand bed was deposited by a faster flow than the 2015 tsunami at Pachingo marsh.

Tsunami deposits can undergo post-depositional alteration, namely erosion, bioturbation, or winnowing of fine sediment that may result in an under-estimation (due to decrease in thickness) or over-estimation (due to a loss of fine sediment) of the flow parameters of the tsunami being modeled (Spiske et al., 2020; Tang and Weiss, 2015). We consider it unlikely that the older sand bed underwent significant alteration following deposition. First, the observed stability of the thickness of the 2015 deposit indicates favorable conditions for preservation at the site; and second, the similarity in the grain size distributions of the 2015 tsunami deposit and the older sand bed suggest that fine sediment was not winnowed from the older sand bed after deposition.

5.4. Using historic evidence to constrain possible earthquake sources for the older sand bed

Based on our maximum scoria-derived age for the deposition of the older sand bed (~1862 CE), and our ^{137}Cs- and ^{210}Pb-derived maximum age constraints for the older sand bed (last ~110 years), we consider north-central Chile tsunamigenic earthquakes in 1880, 1922, and 1943 CE as possible candidates for depositing the older sand bed at the Pachingo marsh (Fig. 7). The tsunami triggered by the great 1730 earthquake likely inundated the Tongoy Bay area to significant heights (Fig. 1d), but it is too old to have deposited the older sand bed. Although far-field tsunamis cannot be ruled out, we found no sedimentological evidence of any far-field tsunamis. Such tsunamis generally have much lower amplitudes than local tsunamis making them less likely to deposit a widespread bed in Pachingo marsh (Satake et al., 2020).

The north-south rupture extents of tsunamigenic north-central Chile earthquakes in 1880 and 1943 were similar to the 2015 north-central Chile earthquake (Fig. 1c). The August 1880 earthquake (M 7.5 to 8) caused some minor damage to cities in north-central Chile, but major damage was focused south of Tongoy Bay (Lomnitz, 1970). Tsunami heights reported in 1880 were lower than 4 m, but accounts are sparse and limited to the Coquimbo area (Fig. 1d). The 1943 earthquake (M_w 7.9) produced building damage further north than the 1880 earthquake. Although reported tsunami heights in 1943 were also lower than 4 m, they were more widespread, making it a better candidate for the deposition of the older sand bed than the 1880 tsunami (Beck et al., 1998; Lomnitz, 1970; Soto et al., 2014). The 1943 rupture is remarkably similar in north-south rupture extent to the 2015 earthquake that produced a significant tsunami at our site.

Beyond the similarity in north-south rupture extent of the 1943 and 2015 earthquakes, there are major differences that set the 1943 and 2015 earthquakes apart. First, the moment calculated for the 1943 earthquake (6×10^{20} Nm; Beck et al., 1998) is ~4 times smaller than for the 2015 earthquake (Carrasco et al., 2019; Tilmann et al., 2016). Second, Tilmann et al. (2016) suggest that the 1943 and 2015 earthquakes had similar down-dip, deep slip, but that the shallow section of the megathrust fault did not rupture in 1943. As a result, it had a smaller moment and produced a smaller tsunami than the 2015 earthquake (Carrasco et al., 2019; Tilmann et al., 2016).

We considered the possibility that the tidal stage during the 1880 and/or 1943 tsunamis may have increased inundation height and extent. However, our tidal modeling indicates that the timing of the 1880 and 1943 tsunamis did not coincide with the highest tides, thus it is unlikely that the tides contributed to increased tsunami heights (Fig. S7). Because historical accounts show that the 1880 and 1943 earthquakes produced relatively smaller tsunami heights than the 2015 earthquake, at least in the Tongoy Bay region, it is unlikely that they produced the older sand bed at our site, which extends ~125 m further inland than the 2015 tsunami deposit (Lomnitz, 1970). For this reason, we conclude that the 1880 and 1943 tsunamis did not deposit the older sand bed.

The 1922 CE northern Chile earthquake (M 8.5–8.6) is a better candidate for the deposition of the older sand bed for several reasons. The 1922 earthquake produced strong shaking and a destructive tsunami along 400 km of the coast from Chañaral to Coquimbo (Lomnitz, 1970; Lockridge, 1985). Tsunami heights were estimated to be between 5 and 7 m above high tide at Caldera and 9 m in Chañaral. At Coquimbo Bay, the tsunami was observed as many sea-level oscillations, with tsunami heights peaking at 4.6 m (Aguirre, 1924). In comparison, the tide gauge at Coquimbo during the 2015 tsunami recorded maximum tsunami heights of ~4.5 m. This makes the 1922 tsunami a good candidate for the deposition of a sand bed in the north-facing Pachingo marsh that exceeded the inland extent of the 2015 tsunami deposit.

In addition, a higher tsunami in 1922 than in 2015 at Pachingo marsh is consistent with the tsunami amplitudes predicted by a simple rupture model of the 1922 earthquake based on macroseismic data (Fig. S8; Beck et al., 1998). As shown in Figure S8, a 400-km-long elliptical-shape rupture area (magnitude 8.5) facing the region severely affected by the earthquake shaking, would produce slightly higher tsunami heights at Pachingo marsh than those predicted by published slip models of the 2015 earthquake. Furthermore, our tidal reconstructions (Fig. S7) show that the tide level during the 1922 tsunami was ~50 cm higher than it was during the 2015 tsunami; again supporting a greater height and inundation from the 1922 tsunami at Pachingo than were experienced in 2015. Taking the above evidence into account, and considering that the time of the 1922 tsunami is consistent with our ^{137}Cs and ^{210}Pb dating, we infer that the 1922 tsunami deposited the older sand bed at the site.

5.5. The influence of Holocene relative sea level on the tsunami record at Pachingo marsh

We attribute the brief tsunami record preserved at Pachingo marsh to the net emergence of the north-central Chile coast during the late Holocene (Garrett et al., 2020; Ota and Paskoff, 1993). Pachingo marsh was a poor recorder of tsunami evidence during the mid-Holocene highstand (~6000 cal yr BP) due to the shallow intertidal or open marine environment of the site (represented by the shell-rich basal sand; May et al., 2013). Following the highstand, sea-level fall and slow tectonic uplift of the coast resulted in shoreline progradation at the site (represented by a series of beach ridges) further limiting the accommodation space necessary to preserve evidence of past tsunamis (Ota and Paskoff, 1993). Over the last two centuries, a significant (~100 m) seaward shift in the shoreline allowed the low-energy, freshwater Pachingo marsh environment to form, which is favorable to the preservation of recent tsunami evidence. Similar brief or fragmentary paleoseismic records attributed to late Holocene sea-level fall have been documented elsewhere in Chile (Atwater et al., 1992; Dura et al., 2016, 2017; Ely et al., 2014; Nelson et al., 2009). We suggest coastlines similar to north-central Chile (e.g., Peru, Oman) that are dominated by siliciclastic sediment may benefit from careful site selection of rare low-energy depositional environments like Pachingo marsh that may contain evidence of past earthquakes and tsunamis.

6. Conclusions

We used stratigraphy, lithology, ^{137}Cs and ^{210}Pb dating, geochemical analysis, historical analysis, and tsunami flow inversion modeling to identify two instances of tsunami inundation at Pachingo marsh in the last ~110 years. By targeting one of the few low energy, organic-rich coastal marshes in north-central Chile inundated during the 2015 tsunami, we were able to identify previous tsunami inundation of the north-central coast.

We conclude that the older sand bed is a tsunami deposit based on its similarity in grain size characteristics to the 2015 tsunami deposit, lateral continuity throughout the site, the upward and landward fining, and a consistent depth in the stratigraphy. The older sand bed can be distinguished from the 2015 tsunami by its farther landward extent and slightly coarser grain size, suggesting it was deposited by a higher and faster flow at Pachingo marsh. The greater relative size of the tsunami that deposited the older sand bed is supported by tsunami flow inversion and tidal modeling, which show higher flow speeds and depths that deposited the older sand bed relative to the 2015 tsunami deposit. ^{137}Cs dating of Pachingo marsh stratigraphy is consistent with the older sand bed having been deposited by the tsunami generated by the 1922 CE earthquake. Historical evidence also suggests that the 1922 tsunami exceeded the size of the 2015 tsunami in Tongoy Bay.

Our identification of the 1922 tsunami deposit and modeling of its inundation are important for earthquake and tsunami hazard assessment along the coast of north-central Chile. Due to the lack of tsunami deposits in this region, hazard assessments for the north-central coast have been limited by sparse historical records. Hazard maps that focus only on potential tsunami inundation from ruptures adjacent to the north-central Chile coast may significantly underestimate the hazard. The addition of the 1922 tsunami to the geologic record of tsunami inundation in this region will improve hazards assessment in this area and help prepare coastal communities for future catastrophic earthquakes and tsunamis.

Author contributions

This project was led by T.D. and J.M.D. J.M.D. and T.D. led the writing of the main text, with contributions from all other authors. T.D. and J.M.D. led fieldwork. J.M.D prepared the figures and tables. H.T., J.M.D., R.W. ran the tsunami flow inversion model. M.C. and M.Ca. provided historical analyses. M.Ca. provided tidal and rupture modeling. J.E.P. ran statistical grain size analysis (PAM). D.R.C contributed cesium and lead dating analysis. B.C.G. advised on geochemical analysis. T.D., J.M.D., B.M., L.L.E., M.C., M.C., H.M.F., C.M., R.L.W., and G.F., were involved with fieldwork.

Declaration of competing interest

The authors declare that they have no known competing financial interests or personal relationships that could have appeared to influence the work reported in this paper.

Acknowledgements

We would like to extend our thanks to Trent Adams for his assistance with sample collection during fieldwork. T.D. was supported by National Science Foundation (NSF) grants EAR-1624795 and EAR-1624533, and L.E. and B.M. were supported by NSF award EAR-1624542. M.C., C.M, G.F., and M.Ca. were supported by the FONDECYT-Chile, project N° 1190258 and by the Millennium Scientific Initiative of the Chilean government through grant NC160025 “Millennium Nucleus CYCLO The Seismic Cycle Along Subduction Zones”. M.Ca acknowledges the support from FONDECYT-Chile, project N° 1181479. This work was supported by the Canadian Foundation for Innovation (CFI-JELF), Canada Research Chair Program, and an NSERC Discovery grant to JP. This is a contribution to the PALSEA (Palaeo-Constraints on Sea-Level Rise), a working group of the International Union for Quaternary Sciences (INQUA) and Past Global Changes (PAGES), and International Geoscience Program (IGCP) International Geoscience Programme (IGCP) Project 725 “Forecasting Coastal Change”. BPH is supported by the Singapore Ministry of Education Academic Research Fund MOE2019-T3-1-004 and MOE2018-T2-1-030, and the National Research Foundation Singapore and the Singapore Ministry of Education under the Research Centers of Excellence initiative. This work comprises EOS contribution number 374. We would also like to thank Alan Nelson, Rob Witter, and an anonymous reviewer for their constructive critiques that helped improve this manuscript. Any use of trade, firm, or product names is for descriptive purposes only and does not imply endorsement by the U.S. Government.

Appendix A. Supplementary data

Supplementary data to this article can be found online at https://doi.org/10.1016/j.quascirev.2021.107052.

References

Aguirre, E., 1924. Informe presentado por el Injeniero don Ernesto Aguirre sobre los materiales i los procedimientos de construcción en la rejión afectada por el terremoto del 10 de noviembre de 1922. In: Anales de la Universidad de Chile. ág-205.

Astaburuaga, F., 1899. Diccionario geográfico de la República de Chile. Segunda Edición Corregida Aumentada 903.

Atwater, B.F., 1987. Evidence for great holocene earthquakes along the outer coast of. Source: Sci. New Ser. 236 (4804), 942–944. http://www.science.earthjay.com/instruction/chemeketa/research_paper/atwater_1987_holocene_earthquakes_washington.pdf.

Atwater, B., Núñez, H., Vita-Finzi, C., 1992. Net Late Holocene emergence despite earthquake-induced submergence, south-central Chile. Quat. Int. 15, 77–85. https://doi.org/10.1016/1040-6182(92)90037-3.

Bahlburg, H., Nentwig, V., Kreutzer, M., 2018. The september 16, 2015 illapel tsunami, Chile – sedimentology of tsunami deposits at the beaches of La serena and Coquimbo. Mar. Geol. 396, 43–53. https://doi.org/10.1016/j.margeo.2016.12.011.

Barnhart, W.D., Murray, J.R., Briggs, R.W., Gomez, F., Miles, C.P.J., Svarc, J., Riquelme, S., Stressler, B.J., 2016. Coseismic slip and early afterslip of the 2015 Illapel, Chile, earthquake: implications for frictional heterogeneity and coastal uplift. J. Geophys. Res.: Solid Earth 121 (8), 6172–6191. https://doi.org/10.1002/2016JB013124.Received.

Beck, S., Barrientos, S., Kausel, E., Reyes, M., 1998. Source characteristics of historic earthquakes along the central Chile subduction zone. J. S. Am. Earth Sci. 11 (2), 115–129. https://doi.org/10.1016/S0895-9811(98)00005-4.

Beyá, J., Álvarez, M., Gallardo, A., Hidalgo, H., Aguirre, C., Valdivia, J., Parra, C., Méndez, L., Contreras, C., Winckler, P., Molina, M., 2016. Atlas De Atlas de Oleaje de Chile. Primera Edit. Econ. 16–26.

Beyá, José, Álvarez, M., Gallardo, A., Hidalgo, H., Winckler, P., 2017. Generation and validation of the Chilean wave atlas database. Ocean Model. 116, 16–32. https://doi.org/10.1016/j.ocemod.2017.06.004.

Blott, S.J., Pye, K., 2001. GRADISTAT: a grain size distribution and statistics package for the analysis of unconsolidated sediments. In: Earth Surface Processes and Landforms, vol. 26, pp. 1237–1248. https://doi.org/10.1016/S0167-5648(08)70015-7. Issue C.

Cable, J.E., Burnett, W.C., Moreland, S.C., Westmoreland, J.B., 2001. Empirical assessment of gamma-ray self absorption in environmental sample analyses. Radioact. Radiochem. 12 (3), 30–41.

Carrasco, S., Ruiz, J.A., Contreras-Reyes, E., Ortega-Culaciati, F., 2019. Shallow intraplate seismicity related to the Illapel 2015 Mw 8.4 earthquake: implications from the seismic source. Tectonophysics 766 (June), 205–218. https://doi.org/10.1016/j.tecto.2019.06.011.

Carvajal, M., Cisternas, M., Gubler, A., Catalán, P.A., Winckler, P., Wesson, R.L., 2017a. Reexamination of the magnitudes for the 1906 and 1922 Chilean earthquakes using Japanese tsunami amplitudes: implications for source depth constraints. J. Geophys. Res.: Solid Earth 122 (1), 4–17. https://doi.org/10.1002/2016JB013269.

Carvajal, M., Cisternas, M., Catalán, P.A., 2017b. Source of the 1730 Chilean earthquake from historical records: Implications for the future tsunami hazard on the coast of Metropolitan Chile. Journal of Geophysical Research: Solid Earth 122 (5), 3648–3660.

Carvajal, M., Contreras-López, M., Winckler, P., Sepúlveda, I., 2017c. Meteotsunamis occurring along the southwest coast of south America during an intense storm. Pure Appl. Geophys. 174 (8), 3313–3323. https://doi.org/10.1007/s00024-017-1584-0.

Cisternas, M., Carvajal, M., Wesson, R., Ely, L.L., Gorigoitia, N., 2017. Exploring the historical earthquakes preceding the giant 1960 Chile earthquake in a time-dependent seismogenic zone. Bull. Seismol. Soc. Am. 107 (6), 2664–2675. https://doi.org/10.1785/0120170103.

Cisternas, Marco, Atwater, B.F., Torrejón, F., Sawai, Y., Machuca, G., Lagos, M., Eipert, A., Youlton, C., Salgado, I., Kamataki, T., Shishikura, M., Rajendran, C.P., Malik, J.K., Rizal, Y., Husni, M., 2005. Predecessors of the giant 1960 Chile earthquake. Nature 437 (7057), 404–407. https://doi.org/10.1038/nature03943.

Comte, D., Eisenberg, A., Lorca, E., Pardo, M., Ponce, L., Saragoni, R., Suárez, G., 1986. The 1985 central Chile earthquake: A repeat of previous great earthquakes in the region? Science 233 (4762), 449–453.

Contreras-Lopez, M., Winkler, P., Sepulveda, I., Andaur-Alvarez, A., Cortes-Molina, F., Guerrero, C.J., Mizobe, C.E., Igualt, F., Breuer, W., Beya, J.F., Vergara, H., Figueroa-Sterquel, R., 2016. Field survey of the 2015 Chile tsunami with emphasis on coastal wetland and conservation areas. Pure Appl. Geophys. 5 (1), 299–319.

Corbett, D.R., Walsh, J.P., 2015. Chapter 24 Lead and 137 Cesium : establishing a chronology for the last century. Handbk. Sea-Level Res. 361–372. https://doi.org/10.1002/9781118452547.ch24.

DeMets, C., Gordon, R.G., Argus, D.F., Stein, S., 1994. Effect of recent revisions to the geomagnetic reversal time scale on estimates of current plate motions. Geophys. Res. Lett. 21 (20), 2191–2194. https://doi.org/10.1029/94GL02118.

Donato, S.V., Reinhardt, E.G., Boyce, J.I., Pilarczyk, J.E., Jupp, B.P., 2009. Particle-size distribution of inferred tsunami deposits in Sur Lagoon, Sultanate of Oman. Mar. Geol. 257 (1–4), 54–64. https://doi.org/10.1016/j.margeo.2008.10.012.

Dura, T., Cisternas, M., Horton, B.P., Ely, L.L., Nelson, A.R., Wesson, R.L., Pilarczyk, J.E., 2015. Coastal evidence for Holocene subduction-zone earthquakes and tsunamis in central Chile. Quat. Sci. Rev. 113, 93–111. https://doi.org/10.1016/j.quascirev.2014.10.015.

Dura, T., Engelhart, S.E., Vacchi, M., Horton, B.P., Kopp, R.E., Peltier, W.R., Bradley, S., 2016. The role of holocene relative sea-level change in preserving records of subduction zone earthquakes. Curr. Clim. Change Rep. 2 (3), 86–100. https://doi.org/10.1007/s40641-016-0041-y.

Dura, T., Horton, B.P., Cisternas, M., Ely, L.L., Hong, I., Nelson, A.R., Wesson, R.L., Pilarczyk, J.E., Parnell, A.C., Nikitina, D., 2017. Subduction zone slip variability during the last millennium, south-central Chile. Quat. Sci. Rev. 175, 112–137. https://doi.org/10.1016/j.quascirev.2017.08.023.

Ely, L.L., Cisternas, M., Wesson, R.L., Dura, T., 2014. Five centuries of tsunamis and land-level changes in the overlapping rupture area of the 1960 and 2010 Chilean earthquakes. Geology 42 (11), 995–998. https://doi.org/10.1130/G35830.1.

Engel, M., Pilarczyk, J.E., May, S.M., Brill, D., Garrett, E., 2020. Geologic Record of Tsunamis and Other Extreme Waves.

Fariña, J.M., He, Q., Silliman, B.R., Bertness, M.D., 2018. Biogeography of salt marsh plant zonation on the Pacific coast of South America. J. Biogeogr. 45 (1),

238–247. https://doi.org/10.1111/jbi.13109.
França, S., Vasconcelos, R.P., Tanner, S., Máguas, C., Costa, M.J., Cabral, H.N., 2011. Assessing food web dynamics and relative importance of organic matter sources for fish species in two Portuguese estuaries: a stable isotope approach. Mar. Environ. Res. 72 (4), 204–215. https://doi.org/10.1016/j.marenvres.2011.09.001.
Fujiwara, O., Kamataki, T., 2007. Identification of tsunami deposits considering the tsunami waveform: an example of subaqueous tsunami deposits in Holocene shallow bay on southern Boso Peninsula. Central Japan 200 (3–4), 295–313. https://doi.org/10.1016/j.sedgeo.2007.01.009.
Garrett, E., Shennan, I., Watcham, E.P., Woodroffe, S.A., 2013. Reconstructing paleoseismic deformation, 1: modern analogues from the 1960 and 2010 Chilean great earthquakes. Quat. Sci. Rev. 75, 11–21. https://doi.org/10.1016/j.quascirev.2013.04.007.
Garrett, E., Shennan, I., Woodroffe, S.A., Cisternas, M., Hocking, E.P., Gulliver, P., 2015. Reconstructing paleoseismic deformation, 2: 1000 years of great earthquakes at Chucalén, south central Chile. Quat. Sci. Rev. 113, 112–122. https://doi.org/10.1016/j.quascirev.2014.10.010.
Garrett, Ed, Melnick, D., Dura, T., Cisternas, M., Ely, L.L., Wesson, R.L., Jara-Muñoz, J., Whitehouse, P.L., 2020. Holocene relative sea-level change along the tectonically active Chilean coast. Quat. Sci. Rev. 236 https://doi.org/10.1016/j.quascirev.2020.106281.
Goto, K., Chagué-Goff, C., Fujino, S., Goff, J., Jaffe, B., Nishimura, Y., Richmond, B., Sugawara, D., Szczuciński, W., Tappin, D.R., Witter, R.C., Yulianto, E., 2011. New insights of tsunami hazard from the 2011 Tohoku-oki event. Mar. Geol. 290 (1–4), 46–50. https://doi.org/10.1016/j.margeo.2011.10.004.
Heinze, B., 2003. Active Intraplate Faulting in the Forearc of North Central Chile, vol. 137.
Hong, I., Dura, T., Ely, L.L., Horton, B.P., Nelson, A.R., Cisternas, M., Nikitina, D., Wesson, R.L., 2017. A 600-year-long stratigraphic record of tsunamis in south-central Chile. Holocene 27 (1), 39–51. https://doi.org/10.1177/0959683616646191.
Horton, B.P., Sawai, Y., Hawkes, A.D., Witter, R.C., 2011. Sedimentology and paleontology of a tsunami deposit accompanying the great Chilean earthquake of February 2010. Marine Micropaleontol. 79 (3–4), 132–138.
Jankaew, K., Atwater, B.F., Sawai, Y., Choowong, M., Charoentitirat, T., Martin, M.E., Prendergast, A., 2008. Medieval forewarning of the 2004 Indian Ocean tsunami in Thailand. Nature 455 (7217), 1228–1231.
Kanamori, H., Rivera, L., Ye, L., Lay, T., Murotani, S., Tsumura, K., 2019. New constraints on the 1922 Atacama, Chile, earthquake from Historical seismograms. Geophys. J. Int. 219 (1), 645–661. https://doi.org/10.1093/gji/ggz302.
Kaufman, L., Rousseeuw, P.J., 1990. Finding Groups in Data: an Introduction to Cluster Analysis. John Wiley & Sons. https://doi.org/10.1002/9780470316801.
Kelsey, H.M., Engelhart, S.E., Pilarczyk, J.E., Horton, B.P., Rubin, C.M., Daryono, M.R., Ismail, N., Hawkes, A.D., Bernhardt, C.E., Cahill, N., 2015. Accommodation space, relative sea level, and the archiving of paleo-earthquakes along subduction zones. Geology 43 (8), 675–678. https://doi.org/10.1130/g36706.1.
Kelsey, H.M., Witter, R.C., Hemphill-Haley, E., 2002. Plate-boundary earthquakes and tsunamis of the past 5500 yr, Sixes River estuary, southern Oregon. Geol. Soc. Am. Bull. 114 (3), 298–314.
Kemp, A.C., Horton, B.P., Vann, D.R., Engelhart, S.E., Grand Pre, C.A., Vane, C.H., Nikitina, D., Anisfeld, S.C., 2012. Quantitative Vertical Zonation of Salt-Marsh Foraminifera for Reconstructing Former Sea Level; an Example from New Jersey, USA, vol. 54, pp. 26–39. https://doi.org/10.1016/j.quascirev.2011.09.014.
Khan, N.S., Vane, C.H., Horton, B.P., 2015. Stable carbon isotope and C/N geochemistry of coastal wetland sediments as a sea-level indicator. Handb. Sea-level Res. 1, 295–311.
León, T., Vargas, G., Salazar, D., Goff, J., Guendon, J.L., Andrade, P., Alvarez, G., 2019. Geo-archaeological records of large Holocene tsunamis along the hyperarid coastal Atacama Desert in the major northern Chile seismic gap. Quat. Sci. Rev. 220, 335–358. https://doi.org/10.1016/j.quascirev.2019.07.038.
Lockridge, P.A., 1985. Tsunamis in Peru-Chile, Vol. 39. The Center.
Lomnitz, C., 1970. Major earthquakes and tsunamis in Chile during the period 1535 to 1955. Geol. Rundsch. 59 (3), 938–960. https://doi.org/10.1007/BF02042278.
Long, W.R., 1930. Railways of south America. Part 3: Chile, p. 373. Trade of Promotion Series, No. 93.
Maechler, M., Rousseeuw, P., Struyf, A., Hubert, M., Hornik, K., 2005. Cluster Analysis Basics and Extensions.
May, S.M., Pint, A., Rixhon, G., Kelletat, D., Wennrich, V., Brückner, H., 2013. Holocene coastal stratigraphy, coastal changes and potential palaeoseismological implications inferred from geo-archives in Central Chile (29–32° S). Z. Für Geomorphol. Suppl. Issues 57 (4), 201–228. https://doi.org/10.1127/0372-8854/2013/s-00154.
Melnick, D., Moreno, M., Motagh, M., Cisternas, M., Wesson, R.L., 2012. Splay fault slip during the Mw 8.8 2010 Maule Chile earthquake. Geology 40 (3), 251–254.
Métois, M., Vigny, C., Socquet, A., Delorme, A., Morvan, S., Ortega, I., Valderas-Bermejo, C.M., 2013. GPS-derived interseismic coupling on the subduction and seismic hazards in the Atacama region, Chile. Geophys. J. Int. 196 (2), 644–655. https://doi.org/10.1093/gji/ggt418.
Melnick, D., Bookhagen, B., Strecker, M.R., 2009. Segmentation of megathrust rupture zones from fore-arc deformation patterns over hundreds to millions of years, Arauco peninsula, Chile. J. Geophys. Res. 114, B01407. https://doi.org/10.1029/2008JB005788. 1.
Morton, R.A., Gelfenbaum, G., Jaffe, B.E., 2007. Physical criteria for distinguishing sandy tsunami and storm deposits using modern examples. Sediment. Geol. 200 (3–4), 184–207. https://doi.org/10.1016/j.sedgeo.2007.01.003.
Muscolo, A., Panuccio, M.R., Piernik, A., 2014. Ecology, distribution and ecophysiology of salicornia europaea L. In: Khan, M.A., Böer, B., Öztürk, M., Al Abdessalaam, T.Z., Clüsener-Godt, M., Gul, B. (Eds.), Sabkha Ecosystems: Volume IV: Cash Crop Halophyte and Biodiversity Conservation. Springer Netherlands, pp. 233–240. https://doi.org/10.1007/978-94-007-7411-7_16.
Nelson, A.R., Briggs, R.W., Dura, T., Engelhart, S.E., Gelfenbaum, G., Bradley, L.A., Forman, S.L., Vane, C.H., Kelley, K.A., 2015. Tsunami recurrence in the eastern Alaska-Aleutian arc: a Holocene stratigraphic record from Chirikof Island, Alaska. Geosphere 11 (4), 1172–1203. https://doi.org/10.1130/GES01108.1.
Nelson, A.R., Hawkes, A.D., Sawai, Y., Engelhart, S.E., Witter, R., Grant-Walter, W.C., Bradley, L.-A., Dura, T., Cahill, N., Horton, B., 2020. Identifying the greatest earthquakes of the past 2000 Years at the nehalem river estuary, northern Oregon coast, USA. Open Quat. 6 https://doi.org/10.5334/oq.70.
Nelson, A.R., Kashima, K., Bradley, L.A., 2009. Fragmentary evidence of great-earthquake subsidence during holocene emergence, Valdivia estuary, South Central Chile. Bull. Seismol. Soc. Am. 99 (1), 71–86. https://doi.org/10.1785/0120080103.
Nentwig, V., Bahlburg, H., Górecka, E., Huber, B., Bellanova, P., Witkowski, A., Encinas, A., 2018. Multiproxy analysis of tsunami deposits-The Tirúa example, central Chile. Geosphere 14 (3), 1067–1086. https://doi.org/10.1130/GES01528.1.
Nittrouer, C.A., Sternberg, R.W., Carpenter, R., Bennett, J.T., 1979. The use of Pb-210 geochronology as a sedimentological tool: application to the Washington continental shelf. Mar. Geol. 31 (3–4), 297–316. https://doi.org/10.1016/0025-3227(79)90039-2.
Ota, Y., Paskoff, R., 1993. Ota and Paskoff 1993 holo SL changes N Chile.pdf. Rev. Geol. Chile 20 (1), 25–32.
Pardo, M., Comte, D., Monfret, T., 2002. Seismotectonic and stress distribution in the central Chile subduction zone. J. S. Am. Earth Sci. 15 (1), 11–22. https://doi.org/10.1016/S0895-9811(02)00003-2.
Pawlowicz, R., Beardsley, B., Lentz, S., 2002. Classical tidal harmonic analysis including error estimates in MATLAB using T_TIDE. Comput. Geosci. 28 (8), 929–937. https://doi.org/10.1016/s0098-3004(02)00013-4.
Pfeiffer, M., Le Roux, Solleiro-Rebolledo, E., Kemnitz, H., Sedov, S., Seguel, O., 2011. Preservation of beach ridges due to pedogenic calcrete development in the Tongoy palaeobay, North-Central Chile. Geomorphology 132 (3–4), 234–248.
Philibosian, B., Meltzner, A.J., 2. Segmentation and supercycles: a catelog of earthquake rupture patterns from the Sumatran Sunda Megathrust and other well-studied faults worldwide. Quat. Sci. Rev. 241.
Pilarczyk, J.E., Horton, B.P., Soria, J.L.A., Switzer, A.D., Siringan, F., Fritz, H.M., Khan, N.S., Ildefonso, S., Doctor, A.A., Garcia, M.L., 2016. Micropaleontology of the 2013 typhoon haiyan overwash sediments from the leyte gulf, Philippines. Sediment. Geol. 339, 104–114. https://doi.org/10.1016/j.sedgeo.2016.04.001.
Saillard, M., Hall, S.R., Audin, L., Farber, D.L., Hérail, G., Martinod, J., Regard, V., Finkel, R.C., Bondoux, F., 2009. Non-steady long-term uplift rates and Pleistocene marine terrace development along the Andean margin of Chile (31°S) inferred from 10Be dating. Earth Planet Sci. Lett. 277 (1–2), 50–63. https://doi.org/10.1016/j.epsl.2008.09.039.
Satake, K., Atwater, B.F., 2007. Long-term perspectives on giant earthquakes and tsunamis at subduction zones. Annu. Rev. Earth Planet. Sci. 35, 349–374.
Satake, K., Heidarzadeh, M., Quiroz, M., Cienfuegos, R., 2020. History and features of trans-oceanic tsunamis and implications for paleo-tsunami studies. Earth Sci. Rev. 202 (January), 103112. https://doi.org/10.1016/j.earscirev.2020.103112.
Sawai, Y., 2020. Subduction zone paleoseismology along the Pacific coast of northeast Japan — progress and remaining problems. Earth Sci. Rev. 208 (March), 103261. https://doi.org/10.1016/j.earscirev.2020.103261.
Sawai, Y., Fujii, Y., Fujiwara, O., Kamataki, T., Komatsubara, J., Okamura, Y., Shishikura, M., 2008. Marine incursions of the past 1500 years and evidence of tsunamis at Suijin-numa, a coastal lake facing the Japan Trench. Holocene 18 (4), 517–528.
Soto, M.V., Märker, M., Rodolfi, G., Sepúlveda, S.A., Cabello, M., 2014. Assessment of geomorphic processes affecting the paleo-landscape of tongoy bay, Coquimbo region, central Chile. Geogr. Fis. Din. Quaternaria 37 (1), 51–66. https://doi.org/10.4461/GFDQ.2014.37.6.
Spiske, M., Piepenbreier, J., Benavente, C., Bahlburg, H., 2013a. Preservation potential of tsunami deposits on arid siliciclastic coasts. Earth Sci. Rev. 126, 58–73. https://doi.org/10.1016/j.earscirev.2013.07.009.
Spiske, M., Piepenbreier, J., Benavente, C., Kunz, A., Bahlburg, H., Steffahn, J., 2013b. Historical tsunami deposits in Peru: sedimentology, inverse modeling and optically stimulated luminescence dating. Quat. Int. 305, 31–44. https://doi.org/10.1016/j.quaint.2013.02.010.
Spiske, M., Tang, H., Bahlburg, H., 2020. Post-depositional alteration of onshore tsunami deposits – implications for the reconstruction of past events. Earth Sci. Rev. 202 (December 2019), 103068. https://doi.org/10.1016/j.earscirev.2019.103068.
Tang, H., Weiss, R., 2015. A model for tsunami flow inversion from deposits (TSUFLIND). Mar. Geol. 370 (July), 55–62. https://doi.org/10.1016/j.margeo.2015.10.011.
Tilmann, F., Zhang, Y., Moreno, M., Saul, J., Eckelmann, F., Palo, M., Deng, Z., Babeyko, A., Chen, K., Baez, J.C., Schurr, B., Wang, R., Dahm, T., 2016. The 2015 Illapel earthquake , central Chile, a type case for a characteristic earthquake? Geophys. Res. Lett. 43, 574–583. https://doi.org/10.1002/2015GL066963.Received.
Troels-Smith, J., 1955. Characterization of Unconsolidated Sediments. https://doi.org/10.1163/_q3_SIM_00374.

Tuttle, M.P., Ruffman, A., Anderson, T., Jeter, H., 2004. Distinguishing tsunami from storm deposits in eastern north America: the 1929 grand banks tsunami versus the 1991 halloween storm. Seismol Res. Lett. 75 (1), 117–131. https://doi.org/10.1785/gssrl.75.1.117.

Udías, A., Madariaga, R., Buforn, E., Muñoz, D., Ros, M., 2012. The large Chilean historical earthquakes of 1647, 1657, 1730, and 1751 from contemporary documents. Bull. Seismol. Soc. Am. 102 (4), 1639–1653. https://doi.org/10.1016/j.ecss.2006.04.019.

Vinagre, C., Salgado, J., Costa, M.J., Cabral, H.N., 2008. Nursery fidelity, food web interactions and primary sources of nutrition of the juveniles of Solea solea and S. senegalensis in the Tagus estuary (Portugal): a stable isotope approach. https://doi.org/10.1016/j.ecss.2007.07.006, 76, 2, 255-264.

Winckler, P.W., Contreras, M., Campos, R.C., Beya, J., Molina, M.M., 2017. El temporal del 8 de agosto de 2015 en las regiones de Valparaiso y Coquimbo, Chile Central. Latin Am. J. Aquat. Res. 45 (4), 622–648. https://doi.org/10.3856/vol45-issue4-fulltext-1.

Woodroffe, C.D., Rogers, K., McKee, K.L., Lovelock, C.E., Mendelssohn, I.A., Saintilan, N., Vermaat, J.E., Thampanya, U., Khan, N.S., Vane, C.H., Horton, B.P., Kemp, A.C., Vane, C.H., Horton, B.P., Culver, S.J., Lamb, A.L., Vane, C.H., Wilson, G.P., Rees, J.G., Megonigal, J.P., 2010. Chapter 20 Stable carbon isotope and C/N geochemistry of coastal wetland sediments as a sea-level indicator. Holocene 69 (10), 623–636. https://doi.org/10.1016/j.ecss.2006.04.019.